

Adaptive Cross-Layer Attention for Image Restoration

Yancheng Wang, Student Member, IEEE,
Ning Xu, Senior Member, IEEE, and Yingzhen Yang, Member, IEEE

Abstract—Non-local attention module has been proven to be crucial for image restoration. Conventional non-local attention processes features of each layer separately, so it risks missing correlation between features among different layers. To address this problem, we aim to design attention modules that aggregate information from different layers. Instead of finding correlated key pixels within the same layer, each query pixel is encouraged to attend to key pixels at multiple previous layers of the network. In order to efficiently embed such attention design into neural network backbones, we propose a novel Adaptive Cross-Layer Attention (ACLA) module. Two adaptive designs are proposed for ACLA: (1) adaptively selecting the keys for non-local attention at each layer; (2) automatically searching for the insertion locations for ACLA modules. By these two adaptive designs, ACLA dynamically selects a flexible number of keys to be aggregated for non-local attention at previous layer while maintaining a compact neural network with compelling performance. Extensive experiments on image restoration tasks, including single image super-resolution, image denoising, image demosaicing, and image compression artifacts reduction, validate the effectiveness and efficiency of ACLA. The code of ACLA is available at <https://github.com/SDL-ASU/ACLA>.

Index Terms—Image restoration, non-local attention, cross-layer attention, key selection, neural architecture search.



1 INTRODUCTION

IMAGE restoration algorithms aim to recover a high-quality image from a contaminated input image by solving an ill-posed image restoration problem. There are various image restoration tasks depending on the type of corruption, such as image denoising [1, 2], demosaicing [1, 3], single image super-resolution [4–6], and image compression artifacts reduction[7]. To restore corrupted information from the contaminated image, a variety of image priors [8–10] were proposed.

Recently, image restoration methods based on deep neural networks have achieved great success. Inspired by the widely used non-local prior, most recent approaches based on neural networks [1, 2] adapt non-local attention into their neural network to enhance the representation learning, following the non-local neural networks [11]. In a non-local block, a response is calculated as a weighted sum over all pixel-wise features on the feature map to account for long-range information. Such a module was initially designed for high-level recognition tasks such as image classification, and it has been proven to be beneficial for low-level vision tasks [1, 2].

Though attention modules have been shown to be effective in boosting performance, most attention modules only explore the correlation among features at the same layer. Actually, features at different intermediate layers encode variant information at different scales and might be helpful to augment the information used in recovering the high-quality image. Motivated by the potential benefit

of exploring feature correlation across intermediate layers, Holistic Attention Network (HAN) [12] is proposed to find the interrelationship among features at hierarchical levels with a Layer Attention Module (LAM). However, LAM assigns a single importance weight to all features at the same layer and neglects the difference in spatial positions of these features. Recent research in omnidirectional representation [13] suggests that exploring the relationship among features at different layers can benefit the representation learning of neural networks. Nevertheless, calculating correlation among features at hierarchical layers is computationally expensive due to the quadratic complexity of dot product attention. The complexity of such cross-layer attention design is increased from $(HW)^2L$ to $(HWL)^2$, where H, W are the height and width of the feature map and L is the number of layers. To handle the limitations of the current attention modules, we propose a novel Adaptive Cross-Layer Attention (ACLA) module for various image restoration tasks.

1.1 Contributions

Our contributions are presented as follows.

First, in order to address the limitation caused by only referring to keys within the same layer in most existing attention modules, ACLA module searches for keys across different layers for each query feature, and each query only attends to a small set of keys at different layers. We name the layers where keys are attended to by a query feature the referred layers of that query.

Second, ACLA selects an adaptive number of keys at each layer for each query, and searches for the optimal insert positions. The two adaptive designs, the adaptive key selection and search for insert positions, are designed for both efficiency and effectiveness of the attention mechanism

- Yancheng Wang and Yingzhen Yang are with School of Computing and Augmented Intelligence, Arizona State University, Tempe, AZ, 85281. E-mail: ywan1053@asu.edu, yingzhen.yang@asu.edu
- Ning Xu is with KuaiShou Technology. E-mail: ningxu01@gmail.com

and they are inspired by neural architecture search. Because a query feature only attend to keys at previous layers where ACLA modules are available, ACLA enables automatic search for referred layers for each query.

To demonstrate the effectiveness of the two adaptive designs, we deploy ACLA modules on a commonly used neural network model, EDSR [14], for image restoration. Extensive experiments on single image super-resolution, image denoising, image compression artifacts reduction, and image demosaicing demonstrate the effectiveness of our approach. Moreover, comprehensive ablation studies are conducted in Section 4.6 to explain the superior performance of ACLA over its competing methods, as well as the superiority of the two adaptive designs for ACLA. In particular, ACLA is compared to the competing attention modules in Section 4.6.2, and ablation study for the two adaptive designs of ACLA is performed in Section 4.6.3. The benefit of automatic search for referred layers is discussed in Section 4.6.5. The visualization of keys selected by ACLA are illustrated in Figure 2 and Figure 5.

This paper is organized as follows. Section 2 introduces the related works including neural networks for image restoration, attention mechanism, and neural architecture search. The detailed formulation of ACLA is introduced in Section 3. The experimental results of ACLA for various image restoration tasks and the ablation studies of ACLA are reported in Section 4. We conclude the paper in Section 5.

2 RELATED WORKS

2.1 Neural Networks for Image Restoration

Adopting neural networks for image restoration has achieved great success by utilizing their power in representation. ARCNN [15] was first proposed to use CNN for compression artifacts reduction. Later, DnCNN [7] uses residual learning and batch normalization to boost the performance of CNN for image denoising. In IRCNN [3], a learned set of CNNs are used as denoising prior for other image restoration tasks. For single image super-resolution [4, 5, 16, 17], even more efforts have been devoted to designing advanced architectures and learning methods. For example, RDN [16] and CARN [18] fuse low-level and high-level features with dense connections to provide richer information and details for reconstructing. Recently, non-local attention [2, 19, 20] is also used to further boost the performance of CNN for image restoration.

2.2 Attention Mechanism

Attention mechanism has been applied to many computer vision tasks, such as image captioning [21, 22] and image classification [23, 24]. Non-local attention [11] was first proposed to capture long-range dependencies for high-level recognition tasks. Recently, several works have proposed to leverage non-local attention for low-level vision tasks. In NLRN [2] a recurrent neural network is proposed to incorporate non-local attention. RNAN [1] proposed a residual local and non-local mask branch to obtain non-local mixed attention. RCAN [25] exploits the interdependencies among feature channels by generating different attention for each channel-wise feature. HAN [12] is proposed to find interrelationships among features at hierarchical levels with a layer

attention module. Besides, some recent works attempt to explore the benefits of transformer-based models for image restoration. IPT [26] is proposed to solve various restoration problems in a multi-task learning framework based on visual Transformer. SwinIR [27] adopts the architecture of Swin Transformer. However, compared with methods using CNN architecture, transformer-based image restoration methods usually use large datasets for training. Specifically, IPT uses ImageNet to pretrain the model. SwinIR adapts a combination of four datasets consisting of over 8000 high-quality images as the training set for the tasks of denoising and compression artifact reduction.

2.3 Neural Architecture Search

Neural Architecture Search (NAS) has attracted lots of attention recently. Early works of NAS adopt heuristic methods such as reinforcement learning [28] and evolutionary algorithm [29]. The search process with such methods requires huge computational resources. Recently, various strategies are designed to reduce the expensive costs including weight sharing [30], progressive search [31] and one-shot search [32, 33]. For example, DARTS [32] firstly relaxes the search space to be continuous and conducts the differentiable search. The architecture parameters and network weights are trained simultaneously by gradient descent to reduce the search time.

Despite the success of NAS methods for classification, dense prediction tasks such as semantic image segmentation and image restoration, usually demand more complicated network architectures. Some recent works have been devoted to exploring hierarchical search space for dense prediction tasks. For example, Auto-DeepLab [34] introduces a hierarchical search space for semantic image segmentation. DCNAS [35] build a densely connected search space to extract multi-level information. HNAS [36] also adopts a hierarchical search space for single image super-resolution.

3 ACLA: ADAPTIVE CROSS-LAYER ATTENTION

We detail the formulation of ACLA in the section. The vanilla non-local attention and the proposed adaptive cross-layer attention are introduced in Section 3.1, and the search for insert positions of ACLA modules is described in Section 3.2.

3.1 Cross-Layer Attention

Vanilla Non-Local Attention. Non-Local (NL) attention [11] is designed to integrate the self-attention mechanism into convolutional neural networks for computer vision tasks. It is usually applied on an input feature map $x \in \mathbb{R}^{H \times W \times C}$ to explore self-similarities among all spatial positions. We reshape x to $N \times C$, $N = H \times W$, where H , W , and C are the height, width, and channel number of the input feature map X . A generic NL attention can be formulated as

$$y_i = \frac{1}{C(x)} \sum_{n=1}^N f(x_i, x_n)g(x_n), \quad (1)$$

where i indexes the spatial position of feature maps. y is the output of NL attention with the same size as x . $f(x_i, x_n)$

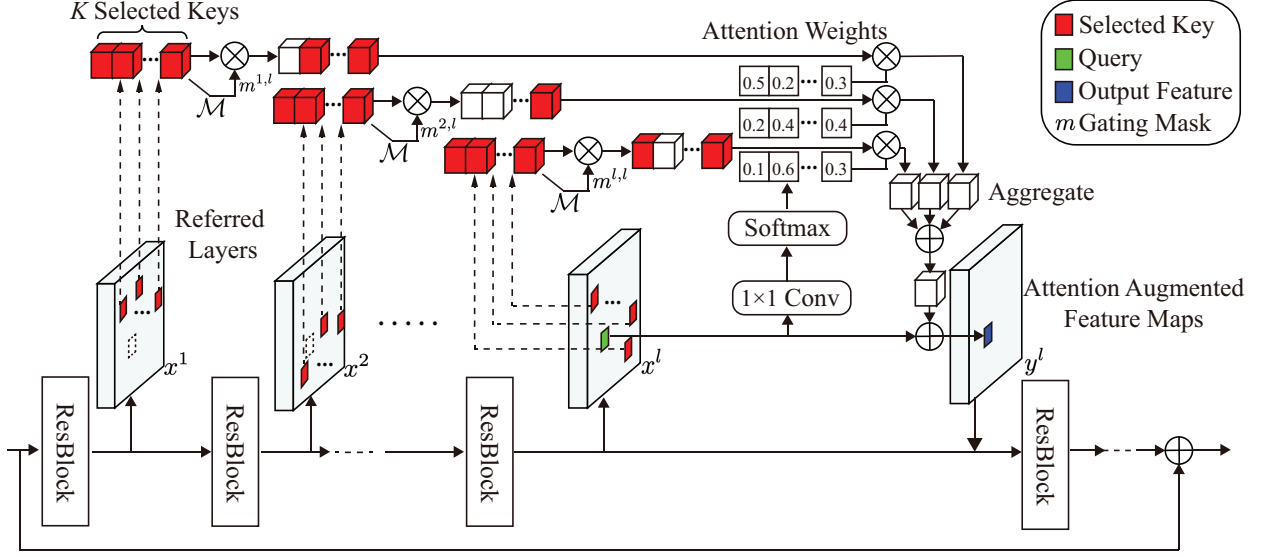


Fig. 1: Illustration of Adaptive Key Selection in an Adaptive Cross-Layer Attention (ACLA) module. For each query pixel, ACLA first selects a fixed number, K , of key features from each referred layer x^j , with j from $\{1, \dots, l\}$. The locations for the selected keys are obtained by applying a 1×1 convolution layer on the query feature. Next, we apply the masking unit \mathcal{M} from Equation(7) to the selected keys to generate the gating masks $\{m^{j,l}\}_{j=1}^l$. By multiplying the gating masks on the selected keys, we achieve adaptive key selection from each referred layer. A convolution layer and Softmax are applied to the query feature to generate attention weights for the selected keys. Weighted by the attention weights, the features of the selected keys are aggregated to the query feature to generate the output of the ACLA module.

is the pairwise affinity between the query feature x_i and its key feature x_n . $g(x_n)$ computes an embedding of feature x_n . $C(x)$ is a normalization term.

NL attention is usually wrapped into a non-local block [11] with a residual connection from the input feature x . The mathematical formulation is given as

$$z = h(y) + x, \quad (2)$$

where h denotes a learnable feature transformation, which takes the output of non-local attention (1) as input.

Adaptive Cross-Layer Attention. To search for keys from different layers for each query feature, we first adapt NL attention in Equation (1) to a cross-layer design, such that features from different layers are regarded as keys.

In the sequel, the superscript indicates the index of a layer, and the subscript indicates spatial location. Suppose that x^i is the output of the i -th layer in a CNN backbone for image restoration, where $i \in \{1, \dots, L\}$ and L is the number of layers. A vanilla Cross-Layer Non-Local (CLNL) attention is formulated as

$$y_i^j = \frac{1}{C(x^j)} \sum_{l=1}^j \sum_{n=1}^N f(x_i^j, x_n^l) g(x_n^l), \quad (3)$$

where the subscripts i, n index the spatial locations of features, the superscripts j, l are the layer indices, and y, x denote the output feature and input feature respectively. With such adaption, relationships among features across different layers can be captured. However, given the quadratic complexity of correlation computation, the complexity of CLNL is increased from N^2L to $(NL)^2$. In order to mitigate the expensive inference cost, we propose to select only a small number, K , of key features from each referred

layer for the attention module, where $K \ll N$. We find the locations of selected keys from each referred layer by learning their offsets from the position of the query feature with the deformable convolution proposed in DCN [37]. As a result, the key features $\{x_n^l\}_{n=1}^N$ in the vanilla CLNL are replaced by $\{x^l(p_i + \Delta p_{ik})\}_{k=1}^K$, where k indexes the sampled keys, and l indexes the referred layer. p_i denotes the 2D spatial position of the query feature x_i^j in the feature map, and Δp_{ik} is the 2-d offset from the position p_i to the position of corresponding sampled key. As $p_i + \Delta p_{ik}$ can be fractional, bilinear interpolation is used as in [37] to compute $x(p_i + \Delta p_{ik})$. To further reduce the computational complexity, we generate the attention weights from the query feature alone by $f(x_i^j)$, where f is a 1×1 convolution followed by a Softmax operation in our work.

With such cross-layer design, each query feature from the input feature map refers to only a fixed number, K , of keys from each previous layer. However, query features at different spatial positions may have different preferences on keys sampled from different layers. The restoration process at different spatial positions may vary significantly due to the diversity of textures in an image, especially for image restoration tasks. As a result, the number of most semantically similar keys at each layer may not be the same across different layers.

To achieve adaptive key selection in the cross-layer attention, we propose Adaptive Cross-Layer Attention (ACLA). Specifically, for each query feature, we dynamically search for the keys sampled from previous layers with ACLA. Besides, when deploying ACLA in CNN backbones, a neural architecture search method is used to search for the insert positions of ACLA. An objective based on the inference cost

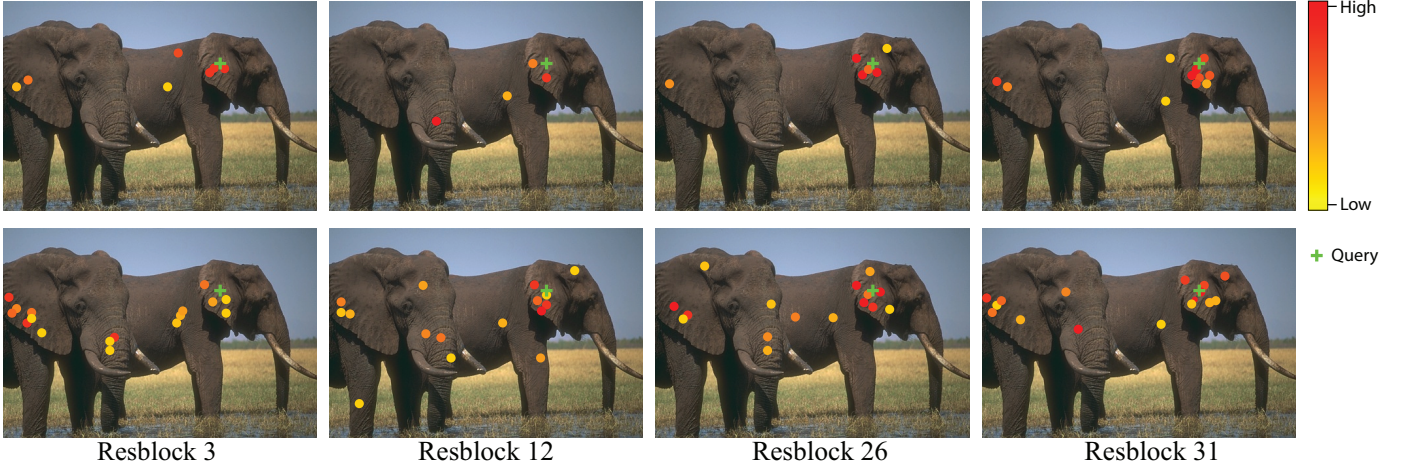


Fig. 2: Visualization of selected keys by ACLA for a query feature from the 31st resblock. The first row shows the positions of the keys selected by ACLA with $K = 16$. For comparison, the positions of keys with top-16 attention weights following the CLNL formulation in Equation (3) is displayed in the second row. From left to right are the sampled key positions from the 3rd, 12th, 26th, and 31st resblock. The query feature is shown as a green cross marker. Each sampled key feature is marked as a circle whose color indicates its attention weight. It can be observed that ACLA adaptively selects semantically similar key features for the query feature, while its vanilla counterpart lacks such capability. More visualization results and analysis can be found in Section 4.7.

of inserted ACLA modules is used to supervise the search procedure.

To search for the informative sampled keys for a query feature from its previous layers, we apply a hard gating mask on the keys sampled from previous layers as

$$y_i^j = \frac{1}{\mathcal{C}(x^j)} \sum_{l=1}^j \sum_{k=1}^K m_{i,k}^{j,l} f(x_i^j) g(x^l(p_i + \Delta p_{ik})), \quad (4)$$

where $m_{i,k}^{j,l}$ is a binary hard gating mask for the k -th sampled key from x^l for query feature x_i^j , whose value is either 1 or 0. Compared to vanilla cross-layer attention, ACLA is more selective when aggregating key features to obtain the output feature. At layer l , it is expected that the most semantically similar keys, which correspond to nonzero $m_{i,k}^{j,l}$, are used to generate the output feature.

To optimize the hard gating mask with gradient descent, we relax the hard gating mask into the continuous domain with the simplified binary Gumbel-Softmax [38]. Thus, the hard gating mask $m_{i,k}^{j,l}$ can be approximated by

$$\hat{m}_{i,k}^{j,l} = \sigma\left(\frac{\beta_{i,k}^{j,l} + \epsilon_{i,k,1}^{j,l} - \epsilon_{i,k,2}^{j,l}}{\tau}\right), \quad (5)$$

where $\hat{m}_{i,k}^{j,l}$ is an approximation of the hard gating mask $m_{i,k}^{j,l}$ in continuous domain. $\beta_{i,k}^{j,l}$ is the sampling parameter. $\epsilon_{i,k,1}^{j,l}, \epsilon_{i,k,2}^{j,l}$ are Gumbel noise for the approximation. τ is the temperature, and σ is the Sigmoid function. During the training, the straight-through estimator from [38, 39] is used for $m_{i,k}^{j,l}$. In the forward pass, the hard gating mask is computed by

$$m_{i,k}^{j,l} = \begin{cases} 1 & \hat{m}_{i,k}^{j,l} > 0.5, \\ 0 & \hat{m}_{i,k}^{j,l} \leq 0.5. \end{cases} \quad (6)$$

In the backward pass, we set $m_{i,k}^{j,l} = \hat{m}_{i,k}^{j,l}$ to enable the regular fractional gradient used in stochastic gradient descent.

The sampling parameter $\beta_{i,k}^{j,l}$ in Equation (5) can be regarded as a soft gating mask, which is used to generate the hard gating mask. To achieve input-dependent key selection, a mask unit \mathcal{M} is used to generate the soft gating mask β from the features of the sampled keys as

$$\beta_{i,k}^{j,l} = \mathcal{M}(x^l(p_i + \Delta p_{ik})). \quad (7)$$

Following the design in [38], a 1×1 convolution layer is used as the mask unit \mathcal{M} in our model. Gumbel noise $\epsilon_{i,l,1}^k$ and $\epsilon_{i,l,2}^k$ are set to 0 during inference. With such a design, we are able to generate a soft gating mask from features of sampled keys and turn it into a hard gating mask to achieve the search for sampled keys based on the input. The overall framework of adaptive key selection in an ACLA module is illustrated in Figure 1.

To demonstrate the effectiveness of adaptive key selection in ACLA, we compare the keys selected by ACLA and those selected by vanilla Cross-Layer Non-Local (CLNL) at different layers for a query feature in Figure 2. It can be observed that semantically similar keys are selected by ACLA for the query feature.

3.2 Insert Positions for ACLA

Insert Positions for ACLA. As demonstrated in Section 4.6.3, the positions where ACLA modules are inserted into the neural backbone have a considerable effect on the final performance. In order to decide the insert positions of ACLA modules in a neural backbone, we propose the following search method. We first densely insert ACLA after each layer of the CNN backbone as shown in Figure 3 to build the supernet. Similar to the gating formulation in ACLA, we define a hard decision parameter $s_l \in \{0, 1\}$ for

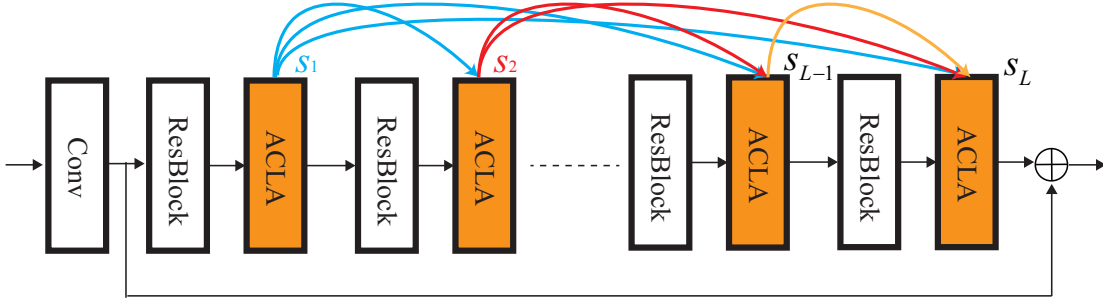


Fig. 3: Illustration of the search for insert positions in ACLA. Except for image super-resolution where the first Conv block is an upscaling block that increases the image resolution, the first Conv block maintains the resolution of the input for the other image restoration tasks.

the l -th inserted ACLA in the supernet. $s_l = 1$ indicates that an ACLA module is inserted after the l -th layer, and $s_l = 0$ otherwise. As a result, the output of ACLA in the supernet can be expressed as

$$y_i^j = \frac{1}{C(x^j)} \sum_{l=1}^j s_l \sum_{k=1}^K m_{i,k}^{j,l} f(x_i^j) g(x^l(p_i + \Delta p_{ik})). \quad (8)$$

It can be observed from (8) that the output of ACLA is the aggregation of features of adaptive keys at previous layers selected by $\{s_l\}$. It is worthwhile to mention that the search for insertion positions enables automatic search for referred layers for each query feature. In particular, the referred layers of a query x_i^j are those of index l with the decision parameter $s_l = 1$ and at least one nonzero mask in the binary hard gating mask $\{m_{i,k}^{j,l}\}$.

The simplified binary Gumbel-Softmax [38] is used here to approximate the hard decision parameter s_l by

$$\hat{s}_l = \sigma\left(\frac{\alpha_l + \epsilon_1 - \epsilon_2}{\tau}\right), \quad (9)$$

with sampling parameter α_l , Gumbel noise ϵ , and temperature τ . Different from the input-dependent design of the gating mask in ACLA, here we directly replace s_l with its continuous approximation \hat{s}_l . α_l here can be regarded as architecture parameters and can be directly optimized by stochastic gradient descent (SGD) during the search process. By gradually decreasing the temperature τ , α_l will be optimized such that s_l will approach 1 or 0.

Search Procedure. To render a compact and efficient neural network with ACLA modules, we need to optimize both the accuracy of a neural network and the inference cost (FLOPs) of the ACLA modules inserted into that neural network. Therefore, the inference cost of the ACLA modules inserted needs to be estimated during the search phase. Following the formulation of the ACLA in the supernet, the inference cost of the ACLA inserted after the j -th residual block as

$$\text{cost}_j = \sum_{l=1}^j s_l \sum_{k=1}^K (2m_{i,k}^{j,l} NC^2 + 2NC^2 + 6KNC), \quad (10)$$

where N is the number of spatial positions, C is the number of channels, K is the maximal number of sampled keys. $2m_{i,k}^{j,l} NC^2$ is the FLOPs for the convolution on generating

the gating masks. $2NC^2 + 6KNC$ is the FLOPs for generating the attention weights and 2D offsets. Then we obtain the inference cost of all inserted ACLA modules as

$$\text{cost} = \sum_{j=1}^L s_j \text{cost}_j. \quad (11)$$

As mentioned before, due to relaxation to continuous problems, we search for the architecture of ACLA, which is comprised of sampled keys at each layer and the insert positions of ACLA modules, by updating the architecture parameters using SGD. The architecture parameters of ACLA are $\alpha = \{\alpha_j\}_{j=1}^L$, where L is the number of layers in the neural network with ACLA. To supervise the search process, we design a loss function with cost-based regularization to achieve multi-objective optimization:

$$\mathcal{L}(w, \alpha) = \mathcal{L}_{MSE} + \lambda \log \text{cost}, \quad (12)$$

where λ is the hyper-parameters that control the magnitude of the cost term.

We find that at the beginning of the search process, ACLA modules inserted at shallow layers are more likely to be maintained. Similar problems has been observed by previous NAS works [40]. To solve this problem, we follow DCNAS [40] and split our search procedure into two stages. In the first stage, we only optimize the parameters of the network for enough epochs to get network weights sufficiently trained. In the second stage, we activate the architecture optimization. We alternatively optimize the network weights by descending $\nabla_w \mathcal{L}_{train}(w, \alpha)$ on the training set, and optimize the architecture parameters by descending $\nabla_\alpha \mathcal{L}_{val}(w, \alpha)$ on the validation set. When the search procedure terminates, we derive the insert positions based on the architecture parameters α .

Differences from Deformable DETR [41]. The proposed ACLA is significantly different from Deformable DETR [41]. Deformable DETR proposes a sparse attention module where each query only attends to a small and fixed set of sampled keys in the input feature map by learning their 2D offsets from the query point. Then, it aggregates the key features selected with the query features. As discussed earlier, Deformable DETR suffers from lack of keys across different layers and lack of flexibility in sampled keys across different layers. It is demonstrated by the ablation studies in Section 4.6.3 and Section 4.6.5 that referring to previous

layers and adaptive key selection improve the performance of attention mechanism compared to baselines without these characteristics.

In contrast with Deformable DETR, each query in ACLA attends to keys from previous layers. Furthermore, ACLA learns hard gating masks for the keys selected from the previous layers. Multiplying the gating masks by the keys selected from the previous layers, each query dynamically selects an adaptive number of keys from each previous layer to attend to. The hard gating masks are obtained by applying Gumbel-Softmax to soft gating masks learned from the query feature in the continuous domain. In addition, the optimal insert positions of ACLA modules are decided using a differentiable neural architecture search algorithm. A set of architecture parameters defined for each layer in the network are learned by optimizing both the MSE loss and the inference cost (FLOPs) of the network. As a result, each query in ACLA attends to an adaptive number of keys from feature maps at selected previous layers.

4 EXPERIMENTS

In this section, we evaluate the performance of ACLA on image restoration tasks, including single image super-resolution, image denoising, image compression artifacts reduction, and image demosaicing. In the implementation, ACLA is deployed on the commonly used neural network model, EDSR [14], for all image restoration tasks. Comparisons with competing methods demonstrate the effectiveness of ACLA. In addition, we perform t-test between ACLA and the current SOTA methods to show the statistical significance of improvement for each task.

4.1 Implementation Details

We use DIV2K [42] as the training set and EDSR [43] as the neural backbones for different image restoration tasks. Following previous works [14, 20, 44], we use EDSR with 32 residual blocks as the backbones for image super-resolution and EDSR with 16 residual blocks as the backbones for image denoising, image compression artifacts reduction, and image demosaicing. In our experiments, ACLA modules are inserted between different residual blocks. DIV2K consists of 800 images for training and 100 images for validation. We follow the training settings in previous works [12, 14, 16, 19] for fair comparisons. We augment the training images by randomly rotating 90° , 180° , 270° , and horizontally flipping. In each mini-batch, 16 low-quality patches with size 48×48 are provided as inputs. ADAM optimizer is used for both the search phase and training phase. Default values of β_1 and β_2 are set to 0.9 and 0.999 respectively, and we set $\epsilon = 10^{-8}$. In the search phase, the learning rate is initialized as 10^{-4} , and the cosine learning rate schedule is used. The search process takes 600 epochs. The first stage of the search takes 300 epochs, and the second stage takes the remaining 300 epochs. In the training phase, the learning rate is initialized as 10^{-4} and the cosine learning rate schedule is used to decay the learning rate to 5×10^{-6} in 800 epochs. For all ACLA modules, the maximum number of selected keys, which is also denoted by K , is initialized as 16. Before the search, we perform a cross-validation on 20%

of the training data to decide the value of λ . Another 10% of training data is held for evaluation in the cross-validation process. The hyper-parameter λ is selected from a candidate set $\{0.1, 0.15, 0.2, 0.25, 0.3, 0.35, 0.4\}$. The selected λ for different tasks are summarized in Table 15.

4.2 Single Image Super-Resolution

For single image super-resolution, we evaluate ACLA on top of the widely used super-resolution backbone EDSR [43]. The LR images are obtained by the bicubic downsampling of HR images. All the methods are evaluated on five standard datasets, Set5 [45], Set14 [46], B100 [47], Urban100 [48], and Manga109 [49]. The reconstructed results by our model are converted to YCbCr space. PSNR and SSIM in the luminance channel are calculated in our experiments. We compare our method with six baseline methods, SRCNN [50], VDSR [51], MemNet [6], SRMDNF [52], RDN [16], SAN [53], HAN [12], NLSN [44], SwinIR [27], and HAT [54]. Note that the results of SwinIR and HAT reported in [27, 54] are obtained by models trained on DIV2K [42] and Flick2K [14]. In our experiments, we train SwinIR and HAT on DIV2K with the same settings as ACLA for fair comparisons. The quantitative results are shown in Table 1. The visual comparisons between ACLA and previous baselines are shown in Figure 4. Our method greatly improves the performance of EDSR on all benchmarks with all upsampling scales. **In particular, the improvements of PSNR over the top baselines NLSN/HAT for $2\times$, $3\times$, and $4\times$ image super-resolution, averaged over all the benchmarks, are 0.118 dB, 0.110 dB, and 0.112 dB respectively.** To verify that such improvement is statistically significant and out of the range of error, we train ACLA and the top baselines, NLSN and HAT, on different super-resolution scales ten times with different seeds for random initialization of the networks. The mean and standard deviation of different runs are shown in Table 5. Then we perform t-test between the results of ACLA and the best among NLSN and HAT on each benchmark dataset with all the super-resolution scales. The largest p-value among all the datasets and super-resolution scales is $0.0021 \ll 0.05$ on Set5 for $2\times$ super-resolution, suggesting that the improvement of ACLA over NLSN is statistically significant.

4.3 Image Denoising

We also evaluate ACLA module on standard benchmarks, KCLDAK24, BSD68 [47], and Urban100 [48], for image denoising. The noisy images are created by adding AWGN noises with $\sigma = 10, 30, 50, 70$. We compare our approach with four baseline methods, DnCNN [7], MemNet [6], RNAN [1], PANet [20], SwinIR [27], SCUNet [55], and Restormer [56]. Note that the results of SwinIR, SCUNet, and Restormer reported in [55, 56] are obtained by models trained on DIV2K [42] and Flick2K [14]. In our experiments, we train SwinIR, SCUNet, and Restormer on DIV2K with the same settings as ACLA for fair comparisons. A 16-layer EDSR is used as the baseline CNN backbone, and ACLA modules are inserted into such neural backbone. We use PSNR as the metric to evaluate different methods. As shown in Table 2, our methods achieve remarkable improvements

TABLE 1: Quantitative results on benchmark datasets for single image super-resolution. The performance of the best baseline is underlined.

Method	Scale	Params(M)	Set5		Set14		B100		Urban100		Manga109	
			PSNR	SSIM	PSNR	SSIM	PSNR	SSIM	PSNR	SSIM	PSNR	SSIM
Bicubic	×2	-	33.66	0.9299	30.24	0.8688	29.56	0.8431	26.88	0.8403	30.80	0.9339
SRCNN	×2	0.244	36.66	0.9542	32.45	0.9067	31.36	0.8879	29.50	0.8946	35.60	0.9663
VDSR	×2	0.672	37.53	0.9590	33.05	0.9130	31.90	0.8960	30.77	0.9140	37.22	0.9750
MemNet	×2	0.677	37.78	0.9597	33.28	0.9142	32.08	0.8978	31.31	0.9195	37.72	0.9740
SRMDNF	×2	5.69	37.79	0.9601	33.32	0.9159	32.05	0.8985	31.33	0.9204	38.07	0.9761
RDN	×2	22.6	38.24	0.9614	34.01	0.9212	32.34	0.9017	32.89	0.9353	39.18	0.9780
SAN	×2	16.7	38.31	0.9620	34.07	0.9213	32.42	0.9028	33.10	0.9370	39.32	0.9792
HAN	×2	17.3	38.27	0.9614	34.16	0.9217	32.41	0.9027	33.35	0.9385	39.46	0.9787
SwinIR	×2	11.8	38.35	0.9620	34.14	0.9227	<u>32.42</u>	<u>0.9030</u>	33.40	0.9393	39.59	0.9790
HAT	×2	24.8	<u>38.34</u>	<u>0.9621</u>	34.11	<u>0.9232</u>	32.40	0.9028	<u>33.52</u>	<u>0.9400</u>	<u>39.60</u>	<u>0.9792</u>
NLSN	×2	44.3	<u>38.34</u>	<u>0.9618</u>	34.08	0.9231	32.43	0.9027	33.42	<u>0.9394</u>	39.59	0.9789
EDSR	×2	40.7	38.11	0.9602	33.92	0.9195	32.32	0.9013	32.93	0.9351	39.10	0.9773
EDSR+NL	×2	43.6	38.15	0.9606	34.00	0.9203	32.37	0.9021	33.05	0.9360	39.21	0.9778
ACLA	×2	42.3	38.39	0.9623	34.24	0.9234	32.55	0.9038	33.56	0.9403	39.77	0.9789
p-value	×2	-	0.0021	-	0.0010	-	1.99e-12	-	3.74e-10	-	1.53e-6	-
Bicubic	×3	-	30.39	0.8682	27.55	0.7742	27.21	0.7385	24.46	0.7349	26.95	0.8556
SRCNN	×3	0.244	32.75	0.9090	29.30	0.8215	28.41	0.7863	26.24	0.7989	30.48	0.9117
VDSR	×3	0.672	33.67	0.9210	29.78	0.8320	28.83	0.7990	27.14	0.8290	32.01	0.9340
MemNet	×3	0.677	34.09	0.9248	30.00	0.8350	28.96	0.8001	27.56	0.8376	32.51	0.9369
SRMDNF	×3	5.69	34.12	0.9254	30.04	0.8382	28.97	0.8025	27.57	0.8398	33.00	0.9403
RDN	×3	22.6	34.71	0.9296	30.57	0.8468	29.26	0.8093	28.80	0.8653	34.13	0.9484
SAN	×3	16.7	34.75	0.9300	30.59	0.8476	29.33	0.8112	28.93	0.8671	34.30	0.9494
HAN	×3	17.3	34.75	0.9299	30.67	0.8483	29.32	0.8110	29.10	0.8705	34.48	0.9500
SwinIR	×3	11.8	34.86	0.9310	30.70	0.8484	29.31	0.8115	29.24	0.8726	34.56	0.9507
HAT	×3	24.8	34.84	0.9305	<u>30.71</u>	<u>0.8485</u>	29.31	0.8116	<u>29.28</u>	<u>0.8728</u>	<u>34.57</u>	<u>0.9509</u>
NLSN	×3	44.3	34.85	0.9306	30.70	<u>0.8485</u>	29.34	0.8117	29.25	0.8726	34.57	0.9508
EDSR	×3	40.7	34.65	0.9280	30.52	0.8462	29.25	0.8093	28.80	0.8653	34.17	0.9476
EDSR+NL	×3	43.6	34.70	0.9291	30.57	0.8470	29.26	0.8102	28.87	0.8670	34.22	0.9484
ACLA	×3	42.3	34.91	0.9312	30.80	0.8494	29.43	0.8127	29.40	0.8734	34.71	0.9516
p-value	×3	-	0.0015	-	0.0003	-	8.98e-8	-	2.44e-9	-	4.64e-6	-
Bicubic	×4	-	28.42	0.8104	26.00	0.7027	25.96	0.6675	23.14	0.6577	24.89	0.7866
SRCNN	×4	0.244	30.48	0.8628	27.50	0.7513	26.90	0.7101	24.52	0.7221	27.58	0.8555
VDSR	×4	0.672	31.35	0.8830	28.02	0.7680	27.29	0.0726	25.18	0.7540	28.83	0.8870
MemNet	×4	0.677	31.74	0.8893	28.26	0.7723	27.40	0.7281	25.50	0.7630	29.42	0.8942
SRMDNF	×4	5.69	31.96	0.8925	28.35	0.7787	27.49	0.7337	25.68	0.7731	30.09	0.9024
RDN	×4	22.6	32.47	0.8990	28.81	0.7871	27.72	0.7419	26.61	0.8028	31.00	0.9151
SAN	×4	16.7	32.64	0.9003	28.92	0.7888	27.78	0.7436	26.79	0.8068	31.18	0.9169
HAN	×4	17.3	32.64	0.9002	<u>28.90</u>	0.7890	<u>27.80</u>	0.7442	26.85	0.8094	<u>31.42</u>	0.9177
SwinIR	×4	11.8	32.65	0.9014	28.89	0.7890	27.78	0.7443	26.95	0.8150	31.33	0.9180
HAT	×4	24.8	<u>32.65</u>	<u>0.9015</u>	28.86	<u>0.7892</u>	27.76	0.7441	26.97	0.8113	31.30	0.9183
NLSN	×4	44.3	32.59	0.9000	28.87	0.7891	27.78	<u>0.7444</u>	26.96	0.8159	31.27	<u>0.9184</u>
EDSR	×4	40.7	32.46	0.8968	28.80	0.7876	27.71	0.7420	26.64	0.8033	31.02	0.9148
EDSR+NL	×4	43.6	32.53	0.8994	28.82	0.7877	27.74	0.7430	26.71	0.8069	31.19	0.9154
ACLA	×4	42.3	32.70	0.9020	28.98	0.7910	27.86	0.7460	27.12	0.8170	31.53	0.9215
p-value	×4	-	0.0012	-	0.0007	-	0.0005	-	4.57e-12	-	3.62e-9	-

TABLE 2: Quantitative results on benchmark datasets for single image denoising

Method	Params (M)	KCLDAk24				BSD68				Urban100			
		10	30	50	70	10	30	50	70	10	30	50	70
MemNet	0.677	N/A	29.67	27.65	26.40	N/A	28.39	26.33	25.08	N/A	28.93	26.53	24.93
DnCNN	0.672	36.98	31.39	29.16	27.64	36.31	30.40	28.01	26.56	36.21	30.28	28.16	26.17
RNAN	7.41	37.24	31.86	29.58	28.16	36.43	30.63	28.27	26.83	36.59	31.50	29.08	27.45
PANet	5.96	37.35	31.96	29.65	28.20	36.50	30.70	28.33	<u>26.89</u>	36.80	31.87	29.47	27.87
SwinIR	11.8	37.38	31.97	<u>29.67</u>	28.20	36.50	30.71	<u>28.35</u>	26.87	36.84	31.88	29.48	27.89
SCUNet	10.8	37.41	31.99	29.65	<u>28.23</u>	<u>36.52</u>	30.71	<u>28.35</u>	26.85	36.87	31.91	29.48	<u>27.90</u>
Restormer	15.8	<u>37.40</u>	31.96	<u>29.67</u>	<u>28.20</u>	36.50	<u>30.73</u>	<u>28.33</u>	26.87	36.85	31.90	<u>29.51</u>	27.89
Baseline	5.43	37.21	31.85	29.60	28.15	36.34	30.60	28.28	26.84	36.63	31.64	29.22	27.54
NL	6.14	37.29	31.90	29.64	28.19	36.43	30.67	28.31	26.89	36.69	31.74	29.30	27.70
ACLA	5.91	37.52	32.10	29.78	28.33	36.65	30.83	28.47	26.99	36.97	31.99	29.63	27.99
p-value	-	3.95e-13	6.75e-9	4.23e-12	3.87e-12	8.19e-11	7.54e-9	5.29e-12	9.31e-11	7.97e-10	2.50e-10	2.97e-11	1.77e-11

on all benchmarks with all noise levels. **The average improvements of PSNR over the top baseline SCUNet for noise levels 10, 30, 50, and 70 are 0.113 dB, 0.103 dB, 0.133 dB, and 0.110 dB.** To verify that such improvement is statistically significant and out of the range of error, we train ACLA and the current SOTA method SCUNet on different noise levels ten times with different seeds for random initial-

ization of the networks. The mean and standard deviation of different runs are shown in Table 6. Then we perform t-test between the results of ACLA and SCUNet on all benchmark datasets with all the noise levels. The largest p-value among all the datasets and noise levels is $7.54e-9 \ll 0.05$ on BSD68 with noise level of 30, suggesting that the improvement of ACLA over SCUNet for image denoising is statistically

TABLE 3: Quantitative results on benchmark datasets for image compression artifacts reduction

Method	Params (M)	LIVE1				Classic5			
		10	20	30	40	10	20	30	40
JPEG	-	27.77	30.07	31.41	32.35	27.82	30.12	31.48	32.43
DnCNN	0.672	29.19	31.59	32.98	33.96	29.40	31.63	32.91	33.77
RNAN	7.41	29.63	32.03	33.45	34.47	29.96	32.11	33.38	34.27
PANet	5.96	29.69	32.10	33.55	34.55	30.03	32.36	33.53	34.38
SwinIR	11.8	29.74	32.13	33.57	34.63	30.06	32.43	33.55	34.42
Baseline	5.43	29.63	32.04	33.50	34.51	29.99	32.22	33.43	34.31
NL	6.14	29.65	32.08	33.55	34.53	30.01	32.34	33.51	34.35
ACLA	5.91	29.83	32.25	33.68	34.71	30.20	32.51	33.67	34.55
p-value	-	8.79e-12	0.0003	0.0002	5.75e-9	8.19e-8	0.0019	0.0024	0.0011

TABLE 4: Quantitative results on benchmark datasets for image demosaicing

Method	Params(M)	McMaster18		Kodak24		BSD68		Urban100	
		PSNR	SSIM	PSNR	SSIM	PSNR	SSIM	PSNR	SSIM
Mosaiced	-	9.17	0.1674	8.56	0.0682	8.43	0.0850	7.48	0.1195
IRCNN	0.731	37.47	0.9615	40.41	0.9807	39.96	0.9850	36.64	0.9743
RNAN	7.41	39.71	0.9725	43.09	0.9902	42.50	0.9929	39.75	0.9848
PANet	5.96	40.00	0.9737	43.29	0.9905	42.86	0.9933	40.50	0.9854
Baseline	5.43	39.81	0.9730	43.18	0.9903	42.66	0.9931	40.23	0.9852
NL	6.14	39.90	0.9732	43.23	0.9903	42.79	0.9932	40.39	0.9853
ACLA	5.91	40.13	0.9749	43.42	0.9917	43.00	0.9950	40.63	0.9864
p-value	-	7.63e-10	-	5.95e-12	-	8.41e-11	-	5.97e-10	-

TABLE 5: PSNR (mean/std) results comparison with p-value between ACLA and top baselines NLSN/HAT for single-image super-resolution

Methods	Scale	Set 5	Set 14	B100	Urban100	Manga109
NLSN	×2	38.34 / 0.0033	34.08 / 0.0030	32.44 / 0.0041	33.42 / 0.0055	39.59 / 0.0056
HAT	×2	38.34 / 0.0033	34.11 / 0.0030	32.40 / 0.0041	33.52 / 0.0055	39.60 / 0.0056
ACLA	×2	38.39 / 0.0029	34.20 / 0.0048	32.55 / 0.0053	33.56 / 0.0070	39.77 / 0.0069
p-value	×2	0.0021	0.0010	1.99e-12	3.74e-10	1.53e-6
NLSN	×3	34.85 / 0.0035	30.70 / 0.0028	29.34 / 0.0049	29.25 / 0.0052	34.57 / 0.0061
HAT	×3	34.84 / 0.0035	30.71 / 0.0028	29.31 / 0.0049	29.28 / 0.0052	34.57 / 0.0061
ACLA	×3	34.91 / 0.0023	30.80 / 0.0033	29.43 / 0.0041	29.40 / 0.0069	34.71 / 0.0046
p-value	×3	0.0015	0.0003	8.98e-8	2.44e-9	4.64e-6
NLSN	×4	32.59 / 0.0027	28.87 / 0.0024	27.78 / 0.0045	26.96 / 0.0060	31.27 / 0.0062
HAT	×4	32.65 / 0.0027	28.86 / 0.0024	27.76 / 0.0045	26.97 / 0.0060	31.30 / 0.0062
ACLA	×4	32.68 / 0.0035	28.98 / 0.0033	27.86 / 0.0051	27.12 / 0.0055	31.53 / 0.0073
p-value	×4	0.0012	0.0007	0.0005	4.57e-12	3.62e-9

TABLE 6: PSNR (mean/std) results comparison with p-value between ACLA and SCUNet for image denoising

Methodos	σ	KCLDAK24	BSD68	Urban100
SCUNet	10	37.41 / 0.0076	36.52 / 0.0077	36.87 / 0.0082
ACLA	10	37.52 / 0.0066	36.65 / 0.0087	36.97 / 0.0085
p-value	10	3.95e-13	8.19e-11	7.97e-10
SCUNet	30	31.99 / 0.0059	30.71 / 0.0061	31.91 / 0.0073
ACLA	30	32.10 / 0.0057	30.83 / 0.0073	31.99 / 0.0059
p-value	30	6.75e-9	7.54e-9	2.50e-10
SCUNet	50	29.65 / 0.0053	28.35 / 0.0084	29.48 / 0.0069
ACLA	50	29.78 / 0.0070	28.47 / 0.0088	29.63 / 0.0079
p-value	50	4.23e-12	5.29e-12	2.97e-11
SCUNet	70	28.21 / 0.0079	26.85 / 0.0084	27.90 / 0.0062
ACLA	70	28.33 / 0.0084	26.99 / 0.0086	27.99 / 0.0086
p-value	70	3.87e-12	9.31e-11	1.77e-11

significant.

4.4 Image Compression Artifacts Reduction

For the task of image compression artifacts reduction (CAR), we compare our methods with DnCNN [7], RNAN [1], PANet [20], and SwinIR [27]. All methods are evaluated on LIVE1 [57] and Classic5 [58]. To obtain the low-quality compressed images, we follow the standard JPEG compression process and use the MATLAB JPEG encoder with quality $q = 10, 20, 30, 40$. For a fair comparison, the results are only evaluated on the Y channel in the YCbCr Space. We also use PSNR as the metric to evaluate different methods. The results are shown in Table 3, where a 16-layer EDSR is used as

the baseline CNN backbone. It can be observed that ACLA boosts the performance of the CNN backbone and surpasses other baseline methods on all the benchmarks at different JPEG compression qualities. **The average improvements of PSNR over the top baseline SwinIR for compression quality 10, 20, 30, and 40 are 0.115 dB, 0.100 dB, 0.115 dB, and 0.105 dB.** To verify that such improvement is statistically significant and out of the range of error, we train ACLA and the current SOTA method SwinIR for different compression qualities ten times with different seeds for random initialization of the networks. The mean and standard deviation of different runs are shown in Table 7. Then we perform t-test between the results of ACLA and SwinIR on all benchmark datasets with all the compression qualities. The largest p-value of the t-test among all the datasets and compression qualities is $0.0024 \ll 0.05$ on Classic5 with compression quality 30, which is much less than 0.05, suggesting that the improvement of ACLA over SwinIR for image compression artifacts reduction is statistically significant.

4.5 Image Demosaicing

For the task of image demosaicing, the evaluation is conducted on Kodak24, McMaster [3], BSD68, and Urban100, following the settings in RNAN [1]. We compare our methods with IRCNN [3], RNAN [1], and PANet [20]. A 16-layer EDSR serves as the baseline CNN model. PSNR is used as the metric to evaluate different methods. As shown in Table

4, ACLA always yields the best reconstruction result for image demosaicing. **The average improvement of PSNR over the top baseline PANet for image demosaicing is 0.135 dB.** To verify that such improvement is statistically significant and out of the range of error, we train ACLA and the current SOTA method PANet ten times with different seeds for random initialization of the networks. The mean and standard deviation of different runs are shown in Table 8. Then we perform t-test between the results of ACLA and PANet on all benchmark datasets with all the compression qualities. The largest p-value of the t-test among all the datasets is $7.63e-10 \ll 0.05$ on McMaster18, suggesting that the improvement of ACLA over PANet for image demosaicing is statistically significant.

4.6 Ablation Study and Discussion

4.6.1 ACLA vs. Non-Local Attention

To verify the effectiveness of our proposed methods, we compare ACLA with the vanilla Non-Local (NL) attention [11] defined in Equation (1) and vanilla Cross-Layer Non-Local (CLNL) attention defined in Equation (3) in terms of computational efficiency and performance. The CLNL follows the formulation in equation (3). The comparison is performed on Set 5 and Set 14 for $2\times$ single image super-resolution with EDSR backbone. The NL and CLNL modules are inserted evenly after every 8th residual block. All the FLOPs in our ablation study are calculated for an input size of 48×48 . Results are presented in Table 9. It can be observed that, with less computation cost, ACLA achieve much better performance compared to standard NL and CLNL modules.

4.6.2 ACLA vs. State-of-the-art Attention Modules

In this subsection, we compare ACLA with several state-of-the-art attention modules that are widely used in the CV community, including Squeeze-and-Excitation (SE) [23] attention and Multi-Head Attention (MHA) [59]. SE models interdependencies between the channels of the convolutional features by re-weighting the channel-wise responses using soft self-attention. MHA is in fact a variant of self-attention from the NLP domain. Specifically, MHA can be regarded as a special non-local attention module that takes account of the relative position information. We insert four SE blocks and four MHA blocks evenly to the EDSR backbone, forming the baseline methods EDSR + SE and EDSR + MHA respectively in Table 10. The comparison is performed for $2\times$ single-image super-resolution on Set 5 and Set 14. The comparative results are shown in Table 10. Although MHA and SE bring improvements over the EDSR baseline, the best results are achieved by our proposed ACLA. Furthermore, we achieve even better performance by inserting a SE block after each ACLA module, as shown in the last row of Table 10.

4.6.3 Ablation Study on the Two Adaptive Designs of ACLA

In Section 3, two adaptive designs are proposed and applied to our ACLA module. The first adaptive design is to select an adaptive number of keys at each layer for non-local attention, and the second adaptive design is to search for optimal insert positions of ACLA modules. To verify the

effectiveness of these two adaptive designs in ACLA, we design a baseline method termed Cross-Layer Attention (CLA). Different from ACLA, the insert positions for CLA are fixed. In our experiment, we insert four CLA modules evenly after every 8th residual block in the EDSR backbone. Each query of CLA refers to a fixed number, that is K , of keys from each previous layer. Thus, the formulation of CLA is $y_i^j = \frac{1}{\mathcal{C}(x^j)} \sum_{l=1}^j \sum_{k=1}^K f(x_i^j)g(x^l(p_i + \Delta p_{ik}))$. Compared to the formulation of ACLA in Equation (8), CLA takes the architecture parameters s_l and $m_{i,k}^{j,l}$ as 1.

To separately verify the effectiveness of the two adaptive designs in ACLA. We further design two baseline modules based on CLA, that are CLA-I and CLA-K. CLA-I stands for CLA with the search for insert positions as that in ACLA. CLA-K stands for CLA which selects an adaptive number of keys at each layer as that in ACLA.

We perform comparison between ACLA, CLA-I, CLA-K, and CLA on Set 5 and Set 14 for $\times 2$ single image super-resolution with EDSR backbone. The comparative results are shown in Table 11. It can be observed that each adaptive design brings improvement on the baseline CLA. ACLA, as a combination of the two adaptive designs, renders better performance than each individual adaptive design.

4.6.4 Ablation Study on the Number of Selected keys K in ACLA

To verify that a small K , which is the maximal number of sampled keys, is sufficient for competitive performance, we compare the performance of ACLA with different values of K . The comparison is performed on Set 5 and Set 14 for $\times 2$ single image super-resolution with EDSR backbone. The results are shown in Table 12. With increased K , the performance of ACLA does not constantly improve. ACLA with $K = 16$ can already achieve comparable performance to those with larger K . This is also consistent with previous studies [60, 61] on the power of sparse representation learning for image restoration.

4.6.5 Ablation Study on Automatic Search for Referred Layers in ACLA

To verify the effectiveness of the automatic search for referred layers in ACLA, we compare ACLA against baselines where queries in each inserted ACLA module refer to keys from the output of a fixed number of preceding layers, which are termed Fixed-Layer ACLA. The comparison is performed on Set 5 and Set 14 for $\times 2$ single image super-resolution using EDSR backbone with 32 residual blocks. The experiment settings are the same as reported in Section 4.1 of our paper. The ACLA modules in Fixed-Layer ACLA are inserted to the same positions in the EDSR backbone as ACLA. However, queries in each ACLA module only refer to keys from the outputs of the previous i residual blocks. When $i = 1$, ACLA with 1 referred layer only refers to keys from the output of the same residual block. When the number of residual blocks previous to an ACLA module is less than i , queries in that ACLA module refer to keys from the outputs of all previous residual blocks. The results in Table 13 show that ACLA outperforms Fixed-Layer ACLA with different number of referred layers. In addition, ACLA

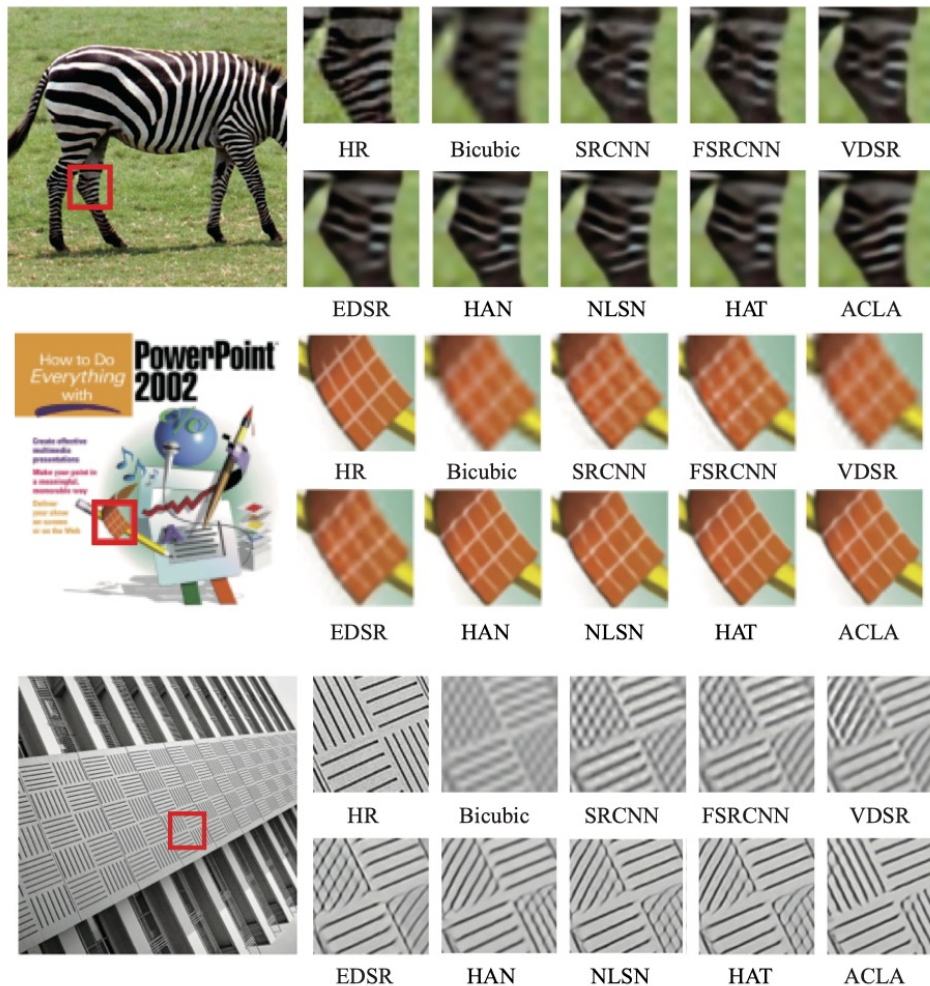


Fig. 4: Visual comparison for $4\times$ SR with BI degradation model.

TABLE 7: PSNR (mean/std) results comparison with p-value between ACLA and SwinIR for image compression artifacts reduction

Method	LIVE1				Classic5			
	10	20	30	40	10	20	30	40
SwinIR	29.74 / 0.0067	32.13 / 0.0073	33.57 / 0.0067	34.63 / 0.0091	30.06 / 0.0061	32.43 / 0.0075	33.55 / 0.0082	34.42 / 0.0083
ACLA	29.83 / 0.0081	32.25 / 0.0066	33.68 / 0.0073	35.55 / 0.0089	30.20 / 0.0077	32.51 / 0.0079	33.67 / 0.0083	34.55 / 0.0082
p-value	8.79e-12	0.0003	0.0002	5.75e-9	8.19e-8	0.0019	0.0024	0.0001

TABLE 8: PSNR (mean/std) results comparison with p-value between ACLA and PANet for image demosaicing

Methods	McMaster18	Kodak24	BSD68	Urban100
PANet	40.00 / 0.0090	43.29 / 0.0118	42.86 / 0.0095	40.50 / 0.0112
ACLA	40.13 / 0.0131	43.42 / 0.0116	43.00 / 0.0117	40.63 / 0.0125
p-value	7.63e-10	5.95e-12	8.41e-11	5.97e-10

TABLE 9: Efficiency comparison with Non-Local attention on Set5

Method	FLOPs(G)	Params(M)	Set 5	Set 14
EDSR	93.97	40.73	38.11	33.92
NL	109.38	43.56	38.15	34.00
CLNL	122.67	45.87	38.14	34.05
ACLA (Ours)	96.97	42.29	38.39	34.24

enjoys less FLOPs and parameter number than the top baseline in Table 13, evidencing the effectiveness and efficiency of automatic search for referred layers in ACLA.

TABLE 10: Efficiency and performance comparison with Squeeze-and-Excitation (SE) attention and Multi-Head Attention (MHA)

Methods	FLOPs(G)	Params(M)	Set 5	Set 14
EDSR	93.97	40.73	38.11	33.92
EDSR + MHA	100.21	42.17	38.23	34.01
EDSR + SE	96.14	41.79	38.19	34.03
EDSR + ACLA	96.97	42.29	38.39	34.24
EDSR + ACLA + SE	99.32	43.47	38.40	34.27

4.6.6 Inference Time Comparison

We compare the inference time between our proposed ACLA and previous state-of-the-art methods based on attention modules. The running time is the average of 100 runs on the input of size 48×48 . We evaluate the running time on a single Tesla V100 16G. We compare our proposed methods with HAN[12], SAN [19], and NLSN [44], which are also attention-based methods for single image super-

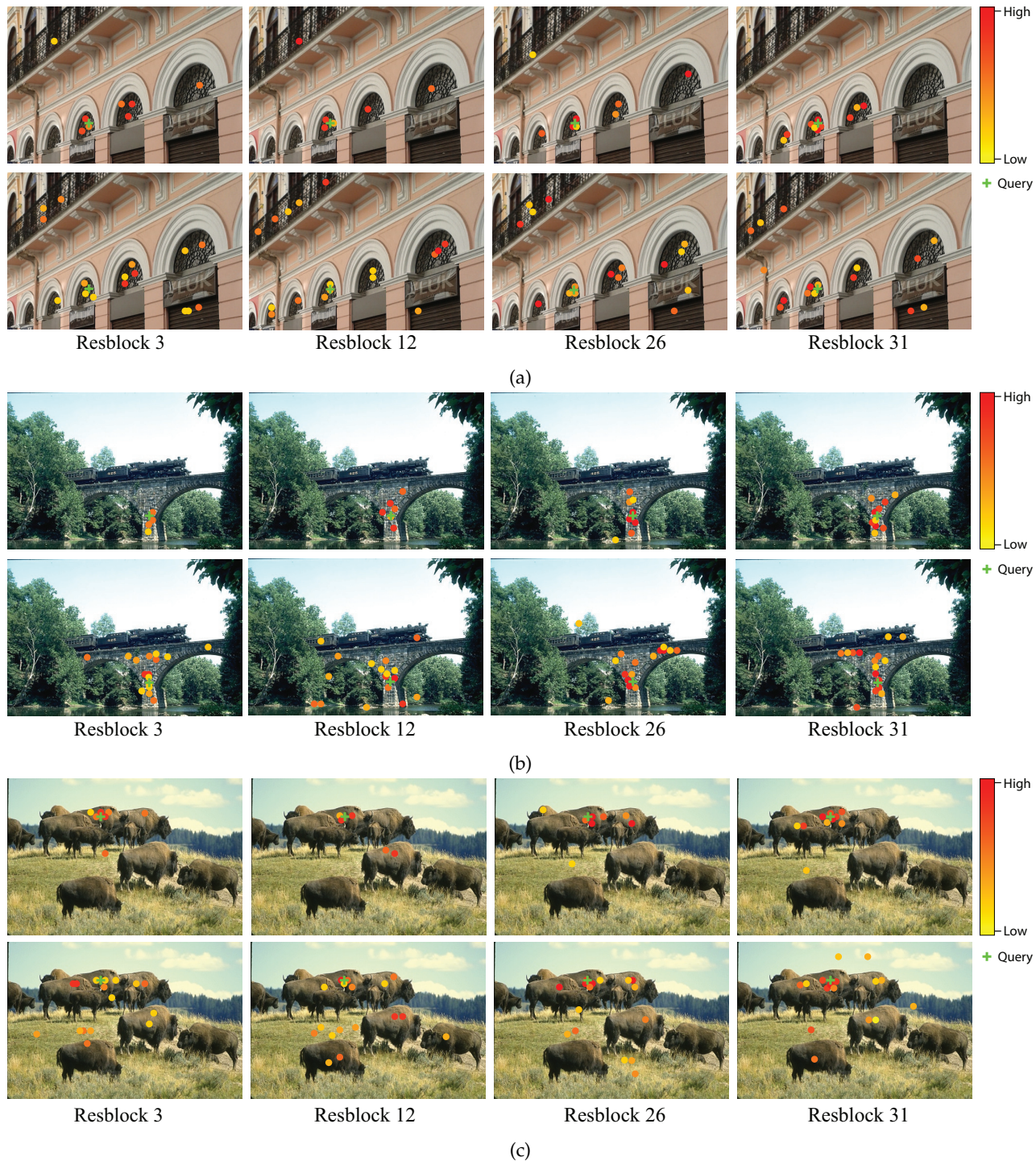


Fig. 5: Visualization of selected keys by ACLA

TABLE 11: Ablation study on the effectiveness of insertion position search and adaptive key selection

Method	FLOPs(G)	Params(M)	Set 5	Set 14
CLA	96.93	42.13	38.27	34.07
CLA-I	96.93	42.13	38.33	34.13
CLA-K	96.87	42.29	38.32	34.15
ACL A	96.97	42.29	38.39	34.24

TABLE 12: Ablation study on number of sampled keys in ACL A on Set5

Method	K	FLOPs(G)	Params(M)	Set 5	Set 14
ACL A	8	96.78	42.18	38.35	34.16
ACL A	16	96.97	42.29	38.39	34.24
ACL A	32	97.56	42.41	38.38	34.25
ACL A	64	98.03	42.69	38.39	34.23
ACL A	128	99.17	43.02	38.37	34.22
ACL A	256	100.59	43.97	38.37	34.24

resolution. As shown in Table 14, EDSR+ACL A achieves better performance than competing methods with less in-

TABLE 13: Ablation study on Automatic Search for Referred Layers in ACLA

Methods	# Referred Layers (i)	FLOPs(G)	Params(M)	Set 5	Set 14
EDSR	-	93.97	40.73	38.11	33.92
Fixed-Layer ACLA	1	94.52	40.92	38.26	34.13
Fixed-Layer ACLA	2	95.13	41.23	38.31	34.15
Fixed-Layer ACLA	4	96.22	41.89	38.33	34.17
Fixed-Layer ACLA	8	101.98	43.94	38.34	34.19
Fixed-Layer ACLA	16	109.79	47.12	38.32	34.17
Fixed-Layer ACLA	32	125.67	54.89	38.34	34.18
ACLA	-	96.97	42.29	38.39	34.24

ference time.

TABLE 14: Inference time comparison

	HAN	SAN	NLSN	EDSR+ACLA
Set 5 (PSNR)	38.27	38.31	38.34	38.39
Time(ms)	38.9	61.2	20.8	19.8

4.6.7 Analysis on Search Results

We summarize the value of λ , i.e., hyper-parameter that controls the magnitude of the inference cost term, for different tasks in Table 15. The insert positions of ACLA in the searched models are also shown in the same table. For experiments with EDSR [43], ACLA modules are inserted after each residual block in the super network. Note that EDSR with 16 residual blocks is used for image denoising, image demosaicing, and image compression artifacts reduction.

TABLE 15: Search settings for ACLA in different image restoration tasks

Task	Backbone	Value of λ	Insert Positions (block number)
Super-Resolution	32-block EDSR	0.15	3, 12, 26, 31, 32
Denoising	16-block EDSR	0.25	2, 5, 9, 12, 15
Demosaicing	16-block EDSR	0.3	2, 5, 11, 13, 16
Artifacts Reduction	16-block EDSR	0.3	2, 7, 9, 13, 16

4.7 Visualization of Selected Keys

We present more examples of visualization of selected keys by ACLA in Figure 5 to demonstrate the superiority of our method in searching for informative keys for the query feature. The visualization is based on our results for $2\times$ image super-resolution. Similar to Figure 2, the first row shows the positions of the keys selected by ACLA with $K = 16$. For comparison, the positions of keys with top-16 attention weights following the vanilla CLNL attention formulation in Equation (3) are displayed in the second row. From left to right are the sampled key positions from the 3rd, 12th, 26th, and 31st residual blocks.

The visualization results show that ACLA adaptively selects semantically similar keys for the query feature, and its vanilla counterpart CLNL lacks such capability. For instance, in Figure 2, the query is from the ear of the elephant on the right side. With ACLA, 60% of the selected keys across are also from the ear of the same elephant. Besides, among the keys selected outside the ear of the same elephant, 5 out of 11 are from the ear of the elephant on the left, which has similar textures as the ear of the elephant on the right. While with CLNL, only 39% of the selected keys are from the ear of the elephant on the right. Similar observations can also be found in Figure 5. In Figure 5 (a), we pick a query point from the frame structure at the top of a gate. With ACLA, 90% of the keys selected are distributed on the frame structures at the top of the gates. While with

CLNL, positions from the gates and the frame structure at the balcony are also given high attention weights. Only 61% of the selected keys are distributed on the frame structures at the top of gates, which may limit the power of attention modules. Similar observations can also be found Figure 5 (b) and Figure 5 (c). In Figure 5 (b), the query is from the bridge in the middle of the image. All the keys selected by ACLA are also from the bridge. In Figure 5 (c), the query is from the back of a yak. Most of the keys selected by ACLA are also located on the body of yaks. While as shown in the second row, CLNL even assigns large attention weights to positions from the grass and the background. Such observations strongly demonstrate the power of ACLA in searching for informative keys across different layers.

5 CONCLUSIONS

In this paper, we propose Adaptive Cross-Layer Attention, or ACLA, which searches for informative keys across different layers for each query feature in attention modules for image restoration. ACLA features two adaptive designs, selecting an adaptive number of keys at each layer and searching for insert positions of the ACLA modules. In particular, each query feature selects adaptive keys at their referred layers. A neural architecture search method is used to search for the insert positions of the ACLA modules so that the neural network with ACLA modules is compact with competitive performance, which also enables automatic search for referred layers for each query feature. Experiments on image restoration tasks including single-image super-resolution, image denoising, image compression artifacts reduction, and image demosaicing validate the effectiveness and efficiency of the proposed ACLA module.

REFERENCES

- [1] Y. Zhang, K. Li, K. Li, B. Zhong, and Y. Fu, "Residual non-local attention networks for image restoration," in *International Conference on Learning Representations*, 2019.
- [2] D. Liu, B. Wen, Y. Fan, C. C. Loy, and T. S. Huang, "Non-local recurrent network for image restoration," in *Advances in Neural Information Processing Systems*, 2018, pp. 1673–1682.
- [3] K. Zhang, W. Zuo, S. Gu, and L. Zhang, "Learning deep cnn denoiser prior for image restoration," in *CVPR*, 2017.
- [4] Y. Fan, J. Yu, D. Liu, and T. S. Huang, "Scale-wise convolution for image restoration," *arXiv preprint arXiv:1912.09028*, 2019.
- [5] W.-S. Lai, J.-B. Huang, N. Ahuja, and M.-H. Yang, "Deep laplacian pyramid networks for fast and accurate super-resolution," in *CVPR*, 2017.
- [6] Y. Tai, J. Yang, X. Liu, and C. Xu, "Memnet: A persistent memory network for image restoration," in *Proceedings of the IEEE international conference on computer vision*, 2017, pp. 4539–4547.
- [7] K. Zhang, W. Zuo, Y. Chen, D. Meng, and L. Zhang, "Beyond a gaussian denoiser: Residual learning of deep cnn for image denoising," *TIP*, 2017.
- [8] A. Buades, B. Coll, and J.-M. Morel, "A non-local algorithm for image denoising," in *CVPR*, 2005.

- [9] D. Zoran and Y. Weiss, "From learning models of natural image patches to whole image restoration," in *2011 International Conference on Computer Vision*. IEEE, 2011, pp. 479–486.
- [10] M. Zontak, I. Mosseri, and M. Irani, "Separating signal from noise using patch recurrence across scales," in *Proceedings of the IEEE Conference on Computer Vision and Pattern Recognition*, 2013, pp. 1195–1202.
- [11] X. Wang, R. Girshick, A. Gupta, and K. He, "Non-local neural networks," in *Proceedings of the IEEE conference on computer vision and pattern recognition*, 2018, pp. 7794–7803.
- [12] B. Niu, W. Wen, W. Ren, X. Zhang, L. Yang, S. Wang, K. Zhang, X. Cao, and H. Shen, "Single image super-resolution via a holistic attention network," in *European Conference on Computer Vision*. Springer, 2020, pp. 191–207.
- [13] Y. Tay, M. Dehghani, V. Aribandi, J. Gupta, P. Pham, Z. Qin, D. Bahri, D.-C. Juan, and D. Metzler, "Omninet: Omnidirectional representations from transformers," *arXiv preprint arXiv:2103.01075*, 2021.
- [14] B. Lim, S. Son, H. Kim, S. Nah, and K. M. Lee, "Enhanced deep residual networks for single image super-resolution," in *The IEEE Conference on Computer Vision and Pattern Recognition (CVPR) Workshops*, July 2017.
- [15] C. Dong, Y. Deng, C. Change Loy, and X. Tang, "Compression artifacts reduction by a deep convolutional network," in *ICCV*, 2015.
- [16] Y. Zhang, Y. Tian, Y. Kong, B. Zhong, and Y. Fu, "Residual dense network for image super-resolution," in *Proceedings of the IEEE conference on computer vision and pattern recognition*, 2018, pp. 2472–2481.
- [17] M. Haris, G. Shakhnarovich, and N. Ukita, "Deep back-projection networks for super-resolution," in *Proceedings of the IEEE conference on computer vision and pattern recognition*, 2018, pp. 1664–1673.
- [18] N. Ahn, B. Kang, and K.-A. Sohn, "Fast, accurate, and lightweight super-resolution with cascading residual network," in *Proceedings of the European Conference on Computer Vision (ECCV)*, 2018, pp. 252–268.
- [19] T. Dai, J. Cai, Y. Zhang, S.-T. Xia, and L. Zhang, "Second-order attention network for single image super-resolution," in *Proceedings of the IEEE conference on computer vision and pattern recognition*, 2019, pp. 11 065–11 074.
- [20] Y. Mei, Y. Fan, Y. Zhang, J. Yu, Y. Zhou, D. Liu, Y. Fu, T. S. Huang, and H. Shi, "Pyramid attention networks for image restoration," *arXiv preprint arXiv:2004.13824*, 2020.
- [21] K. Xu, J. Ba, R. Kiros, K. Cho, A. Courville, R. Salakhudinov, R. Zemel, and Y. Bengio, "Show, attend and tell: Neural image caption generation with visual attention," in *International conference on machine learning*. PMLR, 2015, pp. 2048–2057.
- [22] L. Chen, H. Zhang, J. Xiao, L. Nie, J. Shao, W. Liu, and T.-S. Chua, "Sca-cnn: Spatial and channel-wise attention in convolutional networks for image captioning," in *Proceedings of the IEEE conference on computer vision and pattern recognition*, 2017, pp. 5659–5667.
- [23] J. Hu, L. Shen, and G. Sun, "Squeeze-and-excitation networks," in *Proceedings of the IEEE conference on computer vision and pattern recognition*, 2018, pp. 7132–7141.
- [24] F. Wang, M. Jiang, C. Qian, S. Yang, C. Li, H. Zhang, X. Wang, and X. Tang, "Residual attention network for image classification," in *Proceedings of the IEEE conference on computer vision and pattern recognition*, 2017, pp. 3156–3164.
- [25] Y. Zhang, K. Li, K. Li, L. Wang, B. Zhong, and Y. Fu, "Image super-resolution using very deep residual channel attention networks," in *Proceedings of the European Conference on Computer Vision (ECCV)*, 2018, pp. 286–301.
- [26] H. Chen, Y. Wang, T. Guo, C. Xu, Y. Deng, Z. Liu, S. Ma, C. Xu, C. Xu, and W. Gao, "Pre-trained image processing transformer," in *Proceedings of the IEEE/CVF Conference on Computer Vision and Pattern Recognition*, 2021, pp. 12 299–12 310.
- [27] J. Liang, J. Cao, G. Sun, K. Zhang, L. Van Gool, and R. Timofte, "Swinir: Image restoration using swin transformer," *arXiv preprint arXiv:2108.10257*, 2021.
- [28] B. Zoph and Q. V. Le, "Neural architecture search with reinforcement learning," in *International Conference on Learning Representations (ICLR)*, 2016.
- [29] L. Xie and A. Yuille, "Genetic cnn," in *Proceedings of the IEEE/CVF International Conference on Computer Vision (ICCV)*, 2017.
- [30] H. Pham, M. Guan, B. Zoph, Q. Le, and J. Dean, "Efficient neural architecture search via parameters sharing," in *International Conference on Machine Learning (ICML)*, 2018.
- [31] C. Liu, B. Zoph, M. Neumann, J. Shlens, W. Hua, L.-J. Li, L. Fei-Fei, A. Yuille, J. Huang, and K. Murphy, "Progressive neural architecture search," in *Proceedings of the European conference on computer vision (ECCV)*, 2018, pp. 19–34.
- [32] H. Liu, K. Simonyan, and Y. Yang, "Darts: Differentiable architecture search," in *International Conference on Learning Representations (ICLR)*, 2018.
- [33] S. Xie, H. Zheng, C. Liu, and L. Lin, "Snas: stochastic neural architecture search," in *International Conference on Learning Representations (ICLR)*, 2018.
- [34] C. Liu, L.-C. Chen, F. Schroff, H. Adam, W. Hua, A. L. Yuille, and L. Fei-Fei, "Auto-deeplab: Hierarchical neural architecture search for semantic image segmentation," in *Proceedings of the IEEE/CVF Conference on Computer Vision and Pattern Recognition (CVPR)*, 2019.
- [35] X. Zhang, H. Xu, H. Mo, J. Tan, C. Yang, L. Wang, and W. Ren, "Dcnas: Densely connected neural architecture search for semantic image segmentation," in *Proceedings of the IEEE/CVF Conference on Computer Vision and Pattern Recognition*, 2021, pp. 13 956–13 967.
- [36] Y. Guo, Y. Luo, Z. He, J. Huang, and J. Chen, "Hierarchical neural architecture search for single image super-resolution," *IEEE Signal Processing Letters*, vol. 27, pp. 1255–1259, 2020.
- [37] J. Dai, H. Qi, Y. Xiong, Y. Li, G. Zhang, H. Hu, and Y. Wei, "Deformable convolutional networks," in *Proceedings of the IEEE international conference on computer vision*, 2017, pp. 764–773.
- [38] T. Verelst and T. Tuytelaars, "Dynamic convolutions: Exploiting spatial sparsity for faster inference," in *Proceedings of the IEEE/CVF Conference on Computer Vision*

- and *Pattern Recognition*, 2020, pp. 2320–2329.
- [39] Y. Bengio, N. Léonard, and A. Courville, “Estimating or Propagating Gradients Through Stochastic Neurons for Conditional Computation,” 8 2013. [Online]. Available: <http://arxiv.org/abs/1308.3432>
- [40] J. Fang, Y. Sun, Q. Zhang, Y. Li, W. Liu, and X. Wang, “Densely connected search space for more flexible neural architecture search,” in *Proceedings of the IEEE/CVF Conference on Computer Vision and Pattern Recognition*, 2020, pp. 10 628–10 637.
- [41] X. Zhu, W. Su, L. Lu, B. Li, X. Wang, and J. Dai, “Deformable DETR: deformable transformers for end-to-end object detection,” in *9th International Conference on Learning Representations, ICLR 2021, Virtual Event, Austria, May 3-7, 2021*. OpenReview.net, 2021.
- [42] R. Timofte, E. Agustsson, L. Van Gool, M.-H. Yang, and L. Zhang, “Ntire 2017 challenge on single image super-resolution: Methods and results,” in *Proceedings of the IEEE conference on computer vision and pattern recognition workshops*, 2017, pp. 114–125.
- [43] B. Lim, S. Son, H. Kim, S. Nah, and K. Mu Lee, “Enhanced deep residual networks for single image super-resolution,” in *Proceedings of the IEEE conference on computer vision and pattern recognition workshops*, 2017, pp. 136–144.
- [44] Y. Mei, Y. Fan, and Y. Zhou, “Image super-resolution with non-local sparse attention,” in *Proceedings of the IEEE/CVF Conference on Computer Vision and Pattern Recognition*, 2021, pp. 3517–3526.
- [45] M. Bevilacqua, A. Roumy, C. Guillemot, and M. L. Alberi-Morel, “Low-complexity single-image super-resolution based on nonnegative neighbor embedding,” 2012.
- [46] R. Zeyde, M. Elad, and M. Protter, “On single image scale-up using sparse-representations,” in *International conference on curves and surfaces*, 2010.
- [47] D. Martin, C. Fowlkes, D. Tal, and J. Malik, “A database of human segmented natural images and its application to evaluating segmentation algorithms and measuring ecological statistics,” in *Proceedings Eighth IEEE International Conference on Computer Vision. ICCV 2001*, vol. 2. IEEE, 2001, pp. 416–423.
- [48] J.-B. Huang, A. Singh, and N. Ahuja, “Single image super-resolution from transformed self-exemplars,” in *Proceedings of the IEEE conference on computer vision and pattern recognition*, 2015, pp. 5197–5206.
- [49] Y. Matsui, K. Ito, Y. Aramaki, A. Fujimoto, T. Ogawa, T. Yamasaki, and K. Aizawa, “Sketch-based manga retrieval using manga109 dataset,” *Multimedia Tools and Applications*, vol. 76, no. 20, pp. 21 811–21 838, 2017.
- [50] C. Dong, C. C. Loy, K. He, and X. Tang, “Image super-resolution using deep convolutional networks,” *IEEE transactions on pattern analysis and machine intelligence*, vol. 38, no. 2, pp. 295–307, 2015.
- [51] J. Kim, J. Kwon Lee, and K. Mu Lee, “Accurate image super-resolution using very deep convolutional networks,” in *Proceedings of the IEEE conference on computer vision and pattern recognition*, 2016, pp. 1646–1654.
- [52] K. Zhang, W. Zuo, and L. Zhang, “Learning a single convolutional super-resolution network for multiple degradations,” in *Proceedings of the IEEE Conference on Computer Vision and Pattern Recognition*, 2018, pp. 3262–3271.
- [53] T. Dai, J. Cai, Y. Zhang, S.-T. Xia, and L. Zhang, “Second-order attention network for single image super-resolution,” in *Proceedings of the IEEE conference on computer vision and pattern recognition*, 2019, pp. 11 065–11 074.
- [54] X. Chen, X. Wang, J. Zhou, and C. Dong, “Activating more pixels in image super-resolution transformer,” *CVPR*, 2023.
- [55] K. Zhang, Y. Li, J. Liang, J. Cao, Y. Zhang, H. Tang, R. Timofte, and L. Van Gool, “Practical blind denoising via swin-conv-unet and data synthesis,” *arXiv preprint arXiv:2203.13278*, 2022.
- [56] S. W. Zamir, A. Arora, S. Khan, M. Hayat, F. S. Khan, and M.-H. Yang, “Restormer: Efficient transformer for high-resolution image restoration,” in *Proceedings of the IEEE/CVF Conference on Computer Vision and Pattern Recognition*, 2022, pp. 5728–5739.
- [57] H. R. Sheikh, Z. Wang, L. Cormack, and A. C. Bovik, “Live image quality assessment database release 2 (2005),” 2005.
- [58] A. Foi, V. Katkovnik, and K. Egiazarian, “Pointwise shape-adaptive dct for high-quality denoising and de-blocking of grayscale and color images,” *TIP*, May 2007.
- [59] I. Bello, B. Zoph, A. Vaswani, J. Shlens, and Q. V. Le, “Attention augmented convolutional networks,” in *Proceedings of the IEEE/CVF international conference on computer vision*, 2019, pp. 3286–3295.
- [60] Z. Zhang, Y. Xu, J. Yang, X. Li, and D. Zhang, “A survey of sparse representation: algorithms and applications,” *IEEE access*, vol. 3, pp. 490–530, 2015.
- [61] M. Elad and M. Aharon, “Image denoising via sparse and redundant representations over learned dictionaries,” *IEEE Transactions on Image processing*, vol. 15, no. 12, pp. 3736–3745, 2006.